Mechanical Properties of 30 Year-Old Naturally Corroded Steel Reinforcing Bars

(article starts on next page)

International Journal of Concrete Structures and Materials

CrossMark

Mechanical Properties of 30 Year-Old Naturally Corroded Steel Reinforcing Bars

Ignasi Fernandez[1*] and Carlos G. Berrocal[1,2]

Abstract

The present paper investigates the mechanical response of more than 120 corroded reinforcing bars extracted from a real bridge after 30 years in service. Corrosion was quantified using gravimetric and 3D-laser scanning measurements. An expression to relate the average and critical corrosion levels was found, the latter being the main parameter governing the capacity of corroded bars. Whereas the strength of the material was not affected by corrosion, the ultimate strain decreased sharply. However, strains were not only affected by cross-sectional reduction but also by the shape of the critical pit and necking at failure.

Keywords: corrosion, pit characterization, 3D-scanning, tensile behaviour, reinforced concrete, necking

1 Introduction

Corrosion of reinforcement steel bars remains one of today's most frequent and significant cause of degradation in existing reinforced concrete structures. Chloride ions and carbon dioxide (CO_2) penetrating in the structure from the environment lead to changes in the chemistry of concrete pore solution that can result in the breakdown of the thin protective film, known as the passive layer, that forms on the steel surface in alkaline conditions. Subsequently, active corrosion of reinforcement is thermodynamically favoured leading to the onset of two main deterioration mechanism, namely a reduction of the steel bars cross-sectional area and the volumetric expansion of the generated corrosion products. The effects of steel corrosion become apparent at multiple levels: at a structural level as a reduction of the structure's ultimate load capacity and ability for load redistribution due to the change in failure modes; at a global or sectional level as a decrease of the sectional bending and shear capacity; and at a local or material level as a deterioration of the bond between steel and concrete due to

cover cracking and a modification of the material properties of steel reinforcement.

The effects of steel corrosion become even more critical in the evaluation of the mechanical properties of corroded steel bars. The change of behaviour of corroded steel reinforcement tested under monotonic tensile loads has been attributed to different reasons. At the material level, the non-homogeneous distribution throughout the bar cross-section of the different material phases originated from the modern manufacturing system named TEMPCORE® is often considered a key factor (Apostolopoulos and Papadakis 2008; Apostolopoulos et al. 2006; Fernandez et al. 2016a; Santos and Henriques 2015; Apostolopoulos 2007; Caprili et al. 2018). Additional mechanisms used to explain the modification of the observed mechanical properties of corroded steel bars involve the consideration of geometrical effects derived from the non-uniform reduction of the bar cross-section. These effects include the appearance of a local bending moment due to the shift of the centre of gravity with respect to the original uncorroded cross-section and the stress concentration at the tip of a pit caused by the sudden change in cross-section, also known as the notch effect (Fernandez et al. 2016a, b; Apostolopoulos et al. 2013; Tang et al. 2014). However, due to the strong dependency between these effects and the actual corrosion shape as shown by Zhu et al. (2017; Zhu and François 2014), assuming

*Correspondence: ignasi.fernandez@chalmers.se
[1] Division of Structural Engineering, Chalmers University of Technology, Göteborg 412 96, Sweden
Full list of author information is available at the end of the article

Springer Open

these effects are valid implies that the actual pit shape, i.e. the pit depth and width, as well as the proportion of uniform and pitting corrosion, respectively, will have a non-negligible impact on the actual behaviour of the steel bar. Consequently, considering that most of the existing research has been carried out on artificially corroded reinforcement bars, the validation and potentially an extension of the aforementioned hypotheses to bars corroded under natural conditions, which is of high relevance for the accurate assessment of corroded reinforced concrete structures, is still missing.

The aim of this study is to evaluate the mechanical properties of naturally corroded bars, which were extracted from a real bridge more than 35 years old. This study is part of a larger experimental campaign comprising more than 20 reinforced concrete specimens obtained from the edge beams of the Stallbacka bridge, which was built in 1981 in Sweden (Lundgren et al. 2015; Tahershamsi et al. 2014; Tahershamsi et al. 2017). The edge beams of the bridge, which presented conspicuous rust stains, longitudinal cracking and cover spalling, all of them symptomatic of an advanced corrosion state, had to be replaced after only 30 years in service. The most probable cause for the significant corrosion damage is primarily attributed to the prolonged exposure of the edge beams to chloride-based de-icing salts. The average temperature and relative humidity as measured by meteorological stations in the vicinity of the bridge location ranged between $-1\,°C \pm 5\,°C$ and $82\% \pm 10\%$ RH in winter and $13\,°C \pm 4\,°C$ and 66% RH $\pm 15\%$ RH in summer.

The specimens retrieved from the bridge were initially subjected to a suspended four-point bending test according the setup illustrated in Fig. 1 to determine their structural capacity. Subsequently the tensile reinforcement bars were extracted from non-critical zones, i.e. regions where the bars had not undergone plastic deformation. This work focuses on the characterization of the mechanical behaviour of corroded bars in which the critical pit geometry at the failure cross-section was carefully documented. The main parameters used to describe the tensile behaviour of reinforcement bars as well as the geometrical features of the critical pit section, including pit depth, width and length, remaining bar area and bar perimeter, have been measured and presented as a function of the actual corrosion level of the bars. Subsequently, relations between the observed mechanical properties and the attained corrosion levels at the crtical pit section have been identified and discussed.

2 Description of Experiments
A total of 126 reinforcing steel bar specimens were used in the present study. The bars presented variable corrosion levels ranging from bars without apparent signs of corrosion, considered as reference (uncorroded) specimens, to bars exhibiting a severe form of uniform pitting, representative of advanced stages of chloride-induced

Fig. 1 Test-setup for suspended four-point bending test. Values expressed in mm
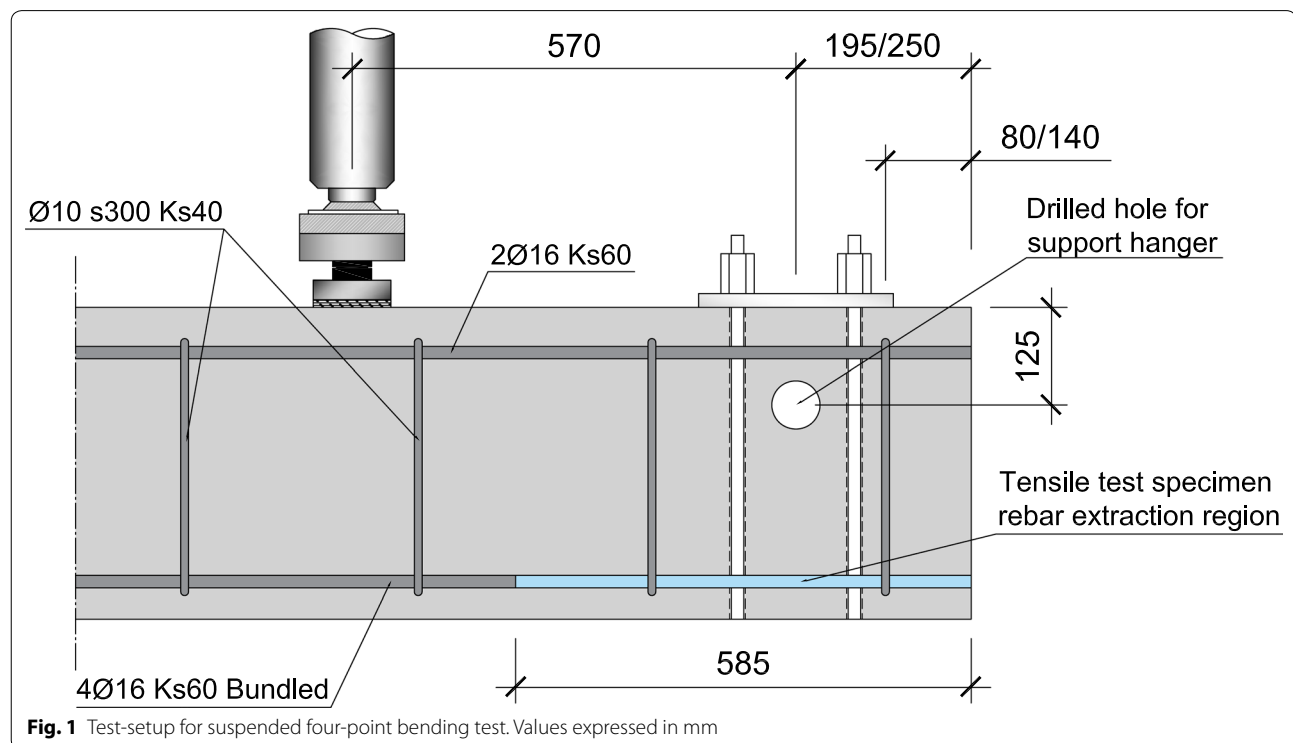
corrosion. The 126 specimens were divided into three different sets: Set-1, integrated by 43 uncorroded bars and Set-2 and Set-3, constituted by a total of 51 and 32 bars, respectively, with variable corrosion levels. The difference between the bars in Set-2 compared to those in Set-3 is that the former were digitally scanned using a 3D-laser scanning technique to get a detailed description of the corroded surface prior tensile testing.
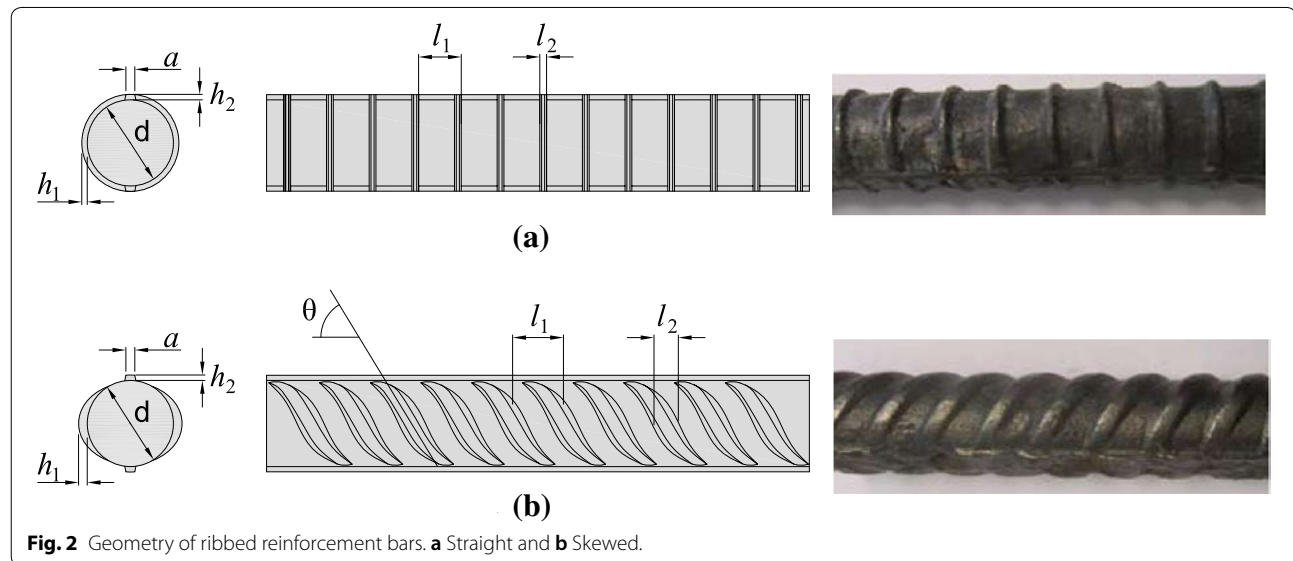
2.1 Geometry of the Reinforcement Bars and Steel Chemical Composition

Over 52 m of reinforcement bar were cut into specimens of three different lengths, namely 300, 400 and 585 mm, respectively. All the specimens were ribbed bars with 16 mm nominal diameter of steel class Ks60 (Institudes and Armeringsstång 1971). However, based on the alignment and distribution of their rib pattern, the reinforcing bars can be divided into two main types: straight (St) and skewed (Sk). The former type presented ribs aligned perpendicular to the bar axis whereas for the latter ones a certain inclination existed between the ribs and the bar axis. Figure 2 illustrates the rib geometry for each bar type together with the nomenclature of the different rib parameters, presented in Table 1, which were measured from the 3D-scanned bar models. Furthermore, the chemical composition of the steel of both bar types, obtained from SEM analysis, is presented in Table 2.

2.2 Corrosion Level Determination
2.2.1 Cleaning Method and Weight Loss Measurement

The cleaning of the bars was performed following the corresponding recommendations specified in the ASTM (2011). Mechanical cleaning through sandblasting was chosen in this study as the preferred cleaning method

Fig. 2 Geometry of ribbed reinforcement bars. **a** Straight and **b** Skewed.

Table 1 Measured parameters describing the geometry of the ribbed reinforcement bars, in mm.

Bar type	Nominal diameter	d	a	h_1	h_2	l_1	l_2	θ (°)
Straight	Ø16	15.77 (0.03)	2.02 (0.18)	1.15 (0.13)	0.72 (0.12)	7.81 (0.08)	2.46 (0.16)	90
Skewed	Ø16	15.62 (0.12)	1.31 (0.04)	1.45 (0.07)	1.53 (0.32)	8.20 (0.11)	5.77 (0.26)	59

Average values and standard deviations (in brackets).

Table 2 Chemical composition of the different bar type steels (% of mass).

Bar type	C	Mn	Si	O	Cr	Ni	Cu	Fe[a]
Straight	2.84	1.08	0.22	4.63	0.19	0.17	0.51	90.36
Skewed	3.05	0.64	0.30	4.52	0.25	0.28	0.32	90.63

[a] Calculated as remainder.

according to the findings reported in (Fernandez et al. 2018). The cleaning of the bars was performed in an individual sandblasting cabinet designed for the purpose. Siliceous sand was employed for the rust removal, which was blasted at approximately 6 bars of pressure. The mass loss was measured after every cycle and reiterated cleaning cycles were applied to each specimen until the marginal mass loss in the last cycle was lower than 0.2% of the initial weight.

2.2.2 3D-Laser Scanning Technique

A detailed description of the steel bars' surface was obtained through 3D-scanning. The scanning of the corroded bars was carried out using a portable laser scanner Handy Scan 700™ from CreaForm®, featuring an accuracy of up to 20 μm and a maximum spatial resolution of the generated point cloud of 50 μm. The outcome of the 3D-scanning procedure consisted of a very fine three-dimensional mesh of triangular elements built upon the nodes of the generated point cloud, see Fig. 3. The average size of the element corresponded to 0.014 mm^2 with a side length of approximately 0.15 mm. The number of triangular elements in each scanning was between $2 \cdot 10^6$

and $3 \cdot 10^6$ elements depending on the level of corrosion. A global coordinate system, (X, Y, Z), was established and referenced to one of the bar ends. The high resolution of the surface mesh allowed for a sufficiently detailed description of the geometry of the bar to obtain information on features including pit depth and length, pit distribution, and loss of cross-sectional area along the bar length, see Fig. 3. It should be noted that a data cleaning operation was performed using the post processing software VXelements before analysing the geometrical features of the bar in order to repair minor defects in the generated mesh such as removing spikes and filling small holes.

2.2.3 Determination of Corrosion Level From the 3D-Scanning Technique

A method developed in a previous study, cf. (Tahershamsi et al. 2016), was used to determine the level of corrosion variation along a bar based on the scanning measurements. Using a script developed in Matlab®, the cross-sectional area of the bar was calculated by integrating the area of the polygons described by the (x, y, z) coordinates of the surface mesh contained
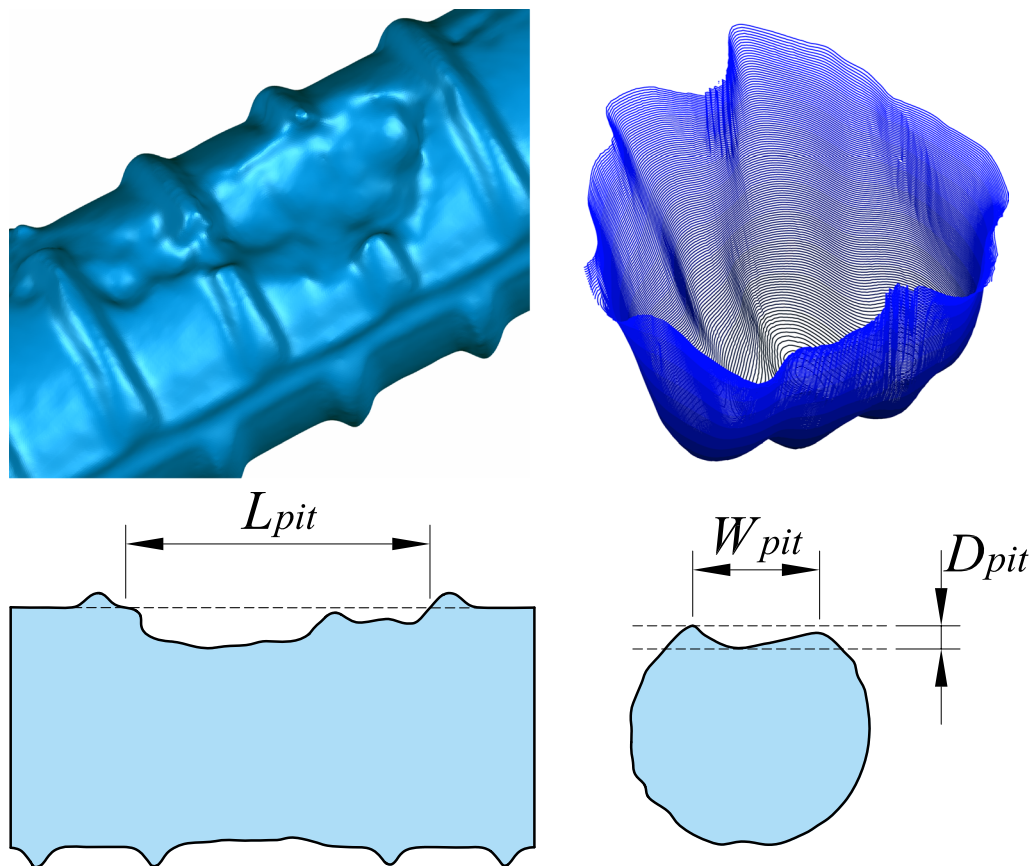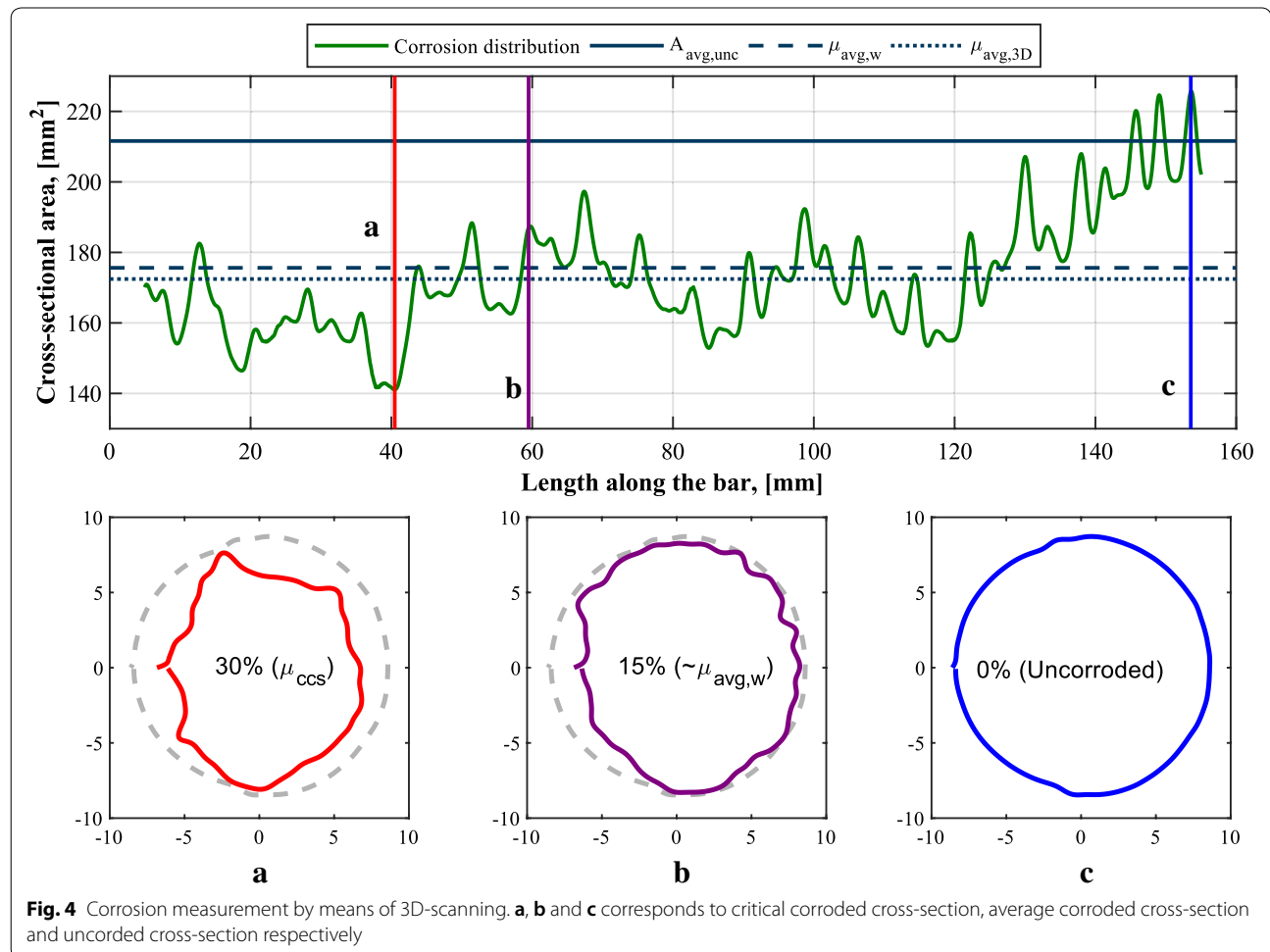

Fig. 3 3D-scanned geometry result and pit characteristics definition.

within planes perpendicular to the bar axis and uniformly spaced at every 0.1 mm. An example of the cross-sectional area variation resulting from this procedure is plotted in Fig. 4. It is worth noting that since the steel bars used in this study possessed ribs, the cross-sectional area along the bars' length exhibits a periodic variation corresponding to the position of the ribs. Three additional cross-sectional magnitudes are included in Fig. 4: (i) the average uncorroded cross-section (determined from uncorroded specimens); (ii) the cross-section corresponding to the average corrosion level based on the 3D-scanning ($\mu_{avg,3D}$); and (iii) the cross-section corresponding to the average corrosion level based on the weight loss measurements ($\mu_{avg,w}$). Furthermore, the cross-section of the bar at three singular locations, namely the critical cross-section (μ_{ccs}), an uncorroded cross-section and a cross-section with an intermediate corrosion level, are also depicted. A detailed description of the steps from the initial 3D-polygonal mesh to the results presented in Fig. 4 is provided in (Tahershamsi et al. 2016).

2.3 Monotonic Tests and Pit Characterisation

Using a MTS Universal Testing machine, all the 126 bars included in this study were subjected to direct monotonic tensile tests, conducted up to failure, according to the standard EN-15630. A length of 65 mm was clamped at each bar end, through which the load was directly applied to the bar. Total machine displacement as well as bar deformation were registered during the tests. The bar deformation was measured using a displacement transducer with a gauge length of 50 mm, which for corroded bars was positioned over the critical pit region. Set-1, consisting of uncorroded bars used to assess the mechanical properties of the reference specimens, was tested under load control, whereas the remaining two sets were tested under displacement control.

The corrosion level of the tested bars ranged between 0 and 19% ($\mu_{avg,w}$). In Fig. 5, a histogram showing the distribution of the number of specimens within the investigated range of corrosion levels is depicted for both straight and skewed bars. Recent studies have attempted to relate the mechanical properties of corroded bars to

Fig. 4 Corrosion measurement by means of 3D-scanning. **a**, **b** and **c** corresponds to critical corroded cross-section, average corroded cross-section and uncorded cross-section respectively

Fig. 5 Corrosion level number of specimens.
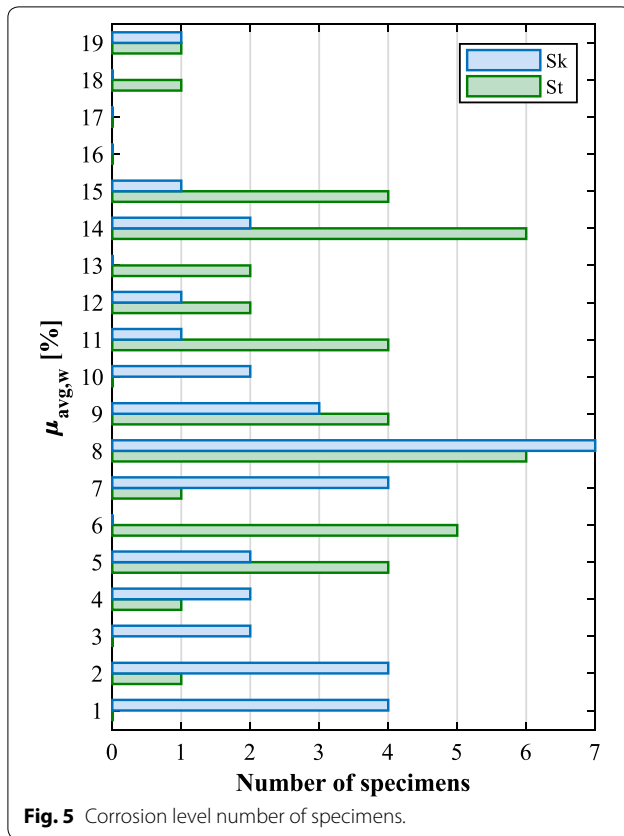
the geometrical features of the critical pit for specimens subjected to accelerated corrosion methods (Apostolopoulos et al. 2013; Fernandez et al. 2015, 2016b; Tang

et al. 2014). In order to perform a similar analysis for naturally corroded bars, the weakest section of each bar was identified prior to testing and the geometrical features defined in this work by pit depth, pit length and pit width, were carefully measured using the 3D-scanned geometry of the bars. Tables 4, 5 and 6, in Appendix A, include all the measured parameters for the specimens in Set-1, Set-2 and Set-3, respectively.

2.4 Mechanical Characterisation of Uncorroded Bars
In order to analyse how corrosion impairs the mechanical properties of reinforcement bars, the mechanical behaviour of uncorroded bars needs to be assessed first. In Fig. 6, the stress–strain curve of the uncorroded specimens is illustrated for both types of bar, including the 90% confidence bounds according to a normal distribution, which highlights the natural dispersion in the material properties. The most representative parameters describing the mechanical behaviour of the bars are illustrated in Fig. 7. Additionally, Table 3 summarises the average value and standard deviation of the main parameters investigated.

3 Corrosion Relationships
The use of a 3D-scanning technique for the obtention of the corrosion level enables a detailed characterisation of the effect of corrosion on the bar surface along the bar length. Accordingly, two different corrosion levels can be defined, which were used in this work to characterise the bars: an average corrosion level ($\mu_{avg,3D}$), calculated as the average of every section created at 0.1 mm spacing along the bar and

Fig. 6 Stress-strain curve for Straight and Skewed uncorroded bars.

Fig. 7 Description of the most relevant parameters of the mechanical properties.
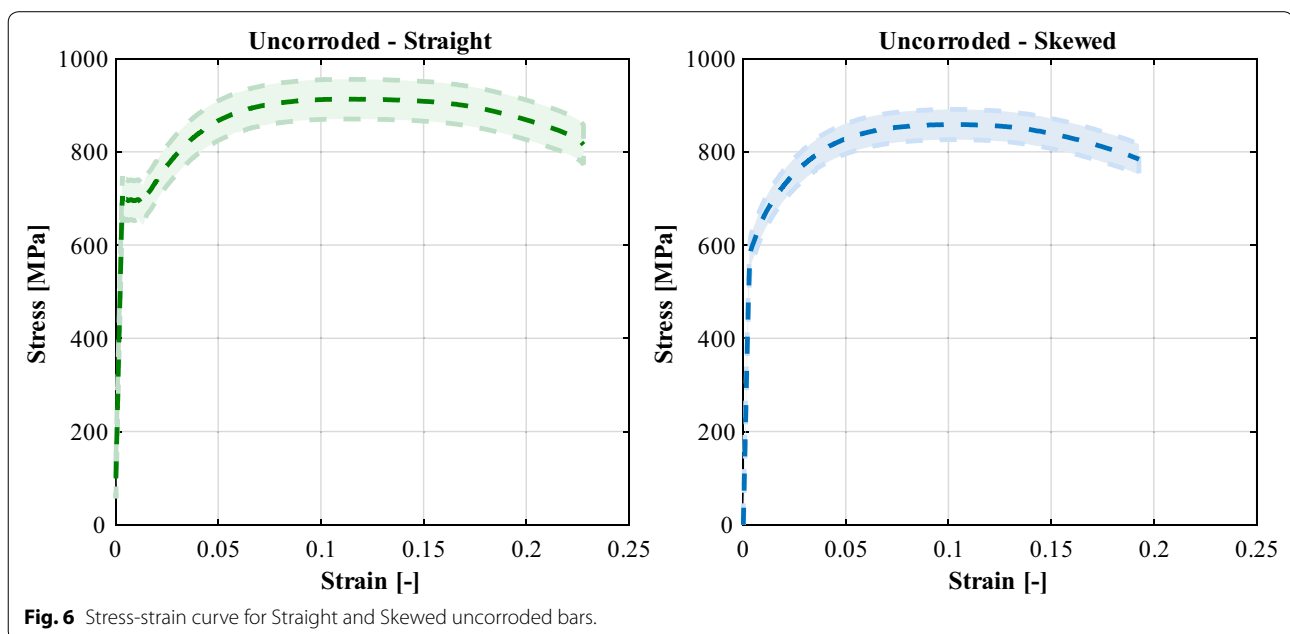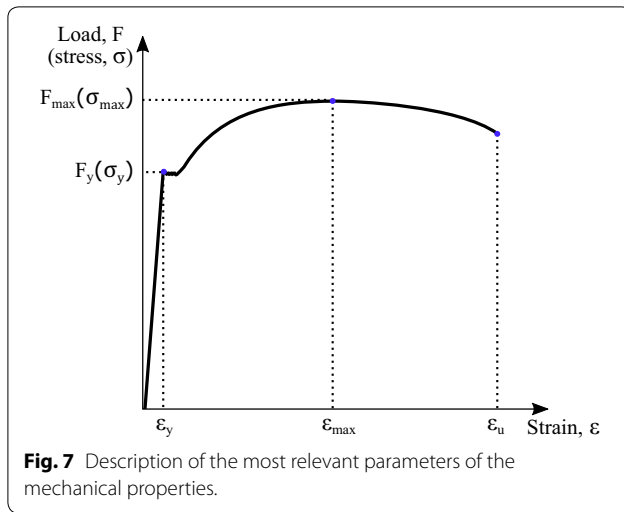
a critical corrosion level (μ_{ccs}), corresponding to the corrosion level of the section with the minimum cross-sectional area obtained from the previous calculation. The section corresponding to the critical corrosion level displays the highest corrosion level in the bar, hence the largest pit and

consequently it is the weakest section where failure is most likely to occur. Since 3D-scanning could be only performed for a portion of the specimens, the relationships between the corrosion level assessed through weight loss measurements and 3D-scanning were investigated in order to establish a relation between both methods. These relations are presented in Fig. 8.

Figure 8a depicts the relation between the average corrosion levels determined by each method, i.e. weight loss and 3D-scanning. Even though small discrepancies were observed, both methods provided comparable results exhibiting values distributed systematically along the equality line. Accordingly, in this work equivalence was assumed between both measurements. On the other hand, when comparing the average weight loss values to the measured critical corrosion levels, the latter were not only consistently higher but also the difference became more apparent as the average corrosion level increased. Nevertheless, an expression, also depicted in Fig. 8b, was found to describe with a reasonable level of agreement the relation between the two different parameters. The expression is defined by Eq. (1) as:

Table 3 Main parameters describing the mechanical properties of uncorroded bars.

Bar type	F_{max} (kN)	F_y (kN)	f_{max} (MPa)	f_y (MPa)	ε_{max} (−)	ε_u (−)	ε_y (−)
Straight	184.2 (9.3)	136.6 (8.5)	865.7 (43.9)	645.5 (40)	0.1117 (0.0009)	0.2184 (0.0115)	0.003
Skewed	179.6 (5.6)	136.3 (5.9)	831.6 (25.7)	630.9 (27)	0.1014 (0.0083)	0.174 (0.035)	0.003

Average values and standard deviations (in brackets).

Fig. 8 Relation between corrosion level measurements.
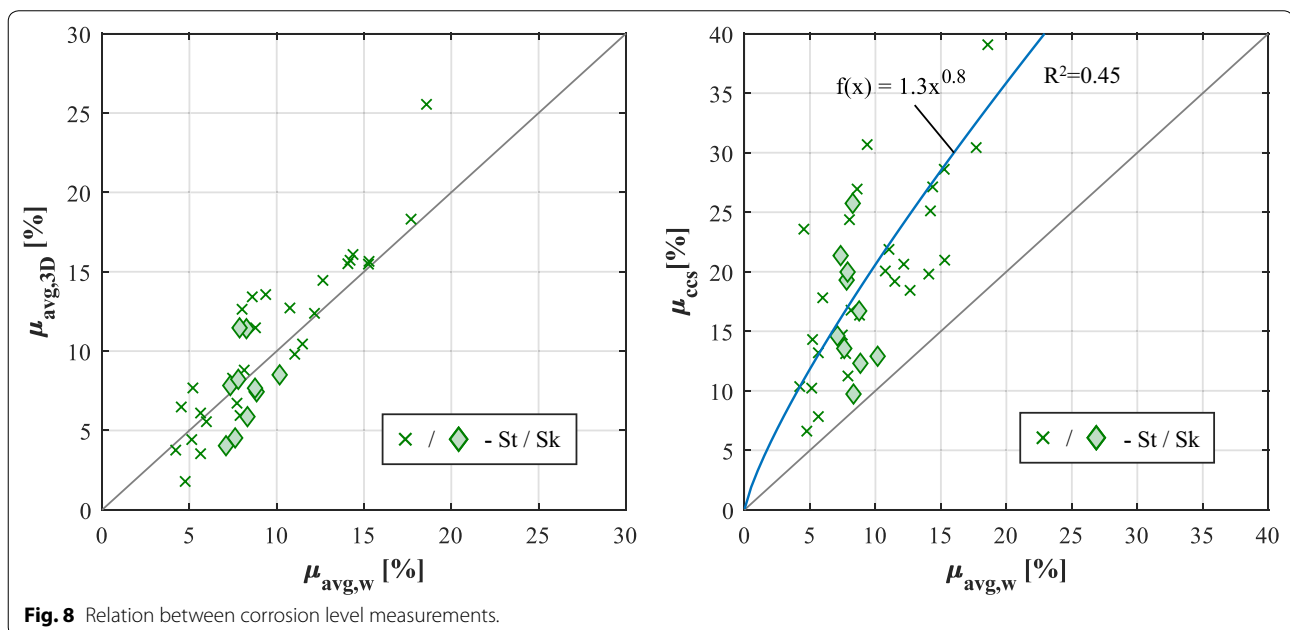
$$y = 1.3 \cdot x^{0.8} \qquad (1)$$

where y corresponds to the μ_{ccs} and x the $\mu_{avg,w}$, both expressed as unit ratios. Using Eq. (1), it is possible to estimate the corrosion level at the most corroded cross-section from an average corrosion level obtained, for instance, from weight loss-measurements. In Sect. 4 a validation for such expression is presented by comparing the experimental test results to the estimated ones for both Set-2 and Set-3.

4 Results and Discussion

This section introduces the results obtained from the tensile tests for the three sets previously described. The complete list of results obtained from the tensile tests can be found in Tables 4, 5 and 6, in Appendix A.

4.1 General Behaviour of the Bars

The curves presented in Fig. 9 display the load-strain behaviour of all the corroded bars included in the presented work. The colour of the curves indicates the average corrosion level ($\mu_{avg,w}$), ranging from 0% corrosion (blue) to 20% corrosion (red). Overall, a general trend can be detected where all the main mechanical parameters are negatively affected by the presence of corrosion; measured load, total displacement and stiffness in corroded bars decreased compared to those of uncorroded values, this reduction being generally proportional to the corrosion level.

4.2 Ultimate and Yielding Load

The results of both the ultimate and the yielding load of the bar are presented Fig. 10. As expected, both magnitudes exhibited a clear reduction with increasing corrosion levels with respect to the reference uncorroded values. However, when plotting the load as a function of the $\mu_{avg,w}$, the loss of load is in almost all cases significantly larger than the theoretical drop of load attributable to the reduction of cross-sectional area due to the corrosion, see Fig. 10a. This phenomenon, already observed in previous research by the authors on bars subjected to accelerated corrosion, cf. (Fernandez et al. 2016b; Imperatore et al. 2017; Zhu et al. 2013), can be described by an expression of the form:

$$F_{corr} = (1 - \alpha \cdot \mu) \cdot F_{unc} \qquad (2)$$

where μ is the corrosion level expressed as a unit ratio, F_{corr} and F_{unc} are the load, either yielding or ultimate, of a corroded and uncorroded bar, respectively, and α is an empirical parameter that controls the degradation rate. A value of α equal to 1 represents the theoretical case when the load decreases proportionally to the corrosion level (solid line in Fig. 10), whereas most reported experimental results have suggested values of α between 1 and 1.8, see e.g. Tang et al. (2014), Imperatore et al. (2017), Zhang et al. (2012), Cairns et al. (2005) and Lu et al. (2016). In the present study, fitting the experimental results to an expression of the form of Eq. (2), yields values of $\alpha_y = 1.36$ and $\alpha_u = 1.43$, which fall within the previously mentioned range.

A noteworthy observation is that in previous investigations where bars of the type TEMPCORE® had been

Fig. 9 Load-strain curve for different corrosion levels.

Fig. 10 Load versus corrosion level. **a** $\mu_{avg,w}$, **b** μ_{ccs}.
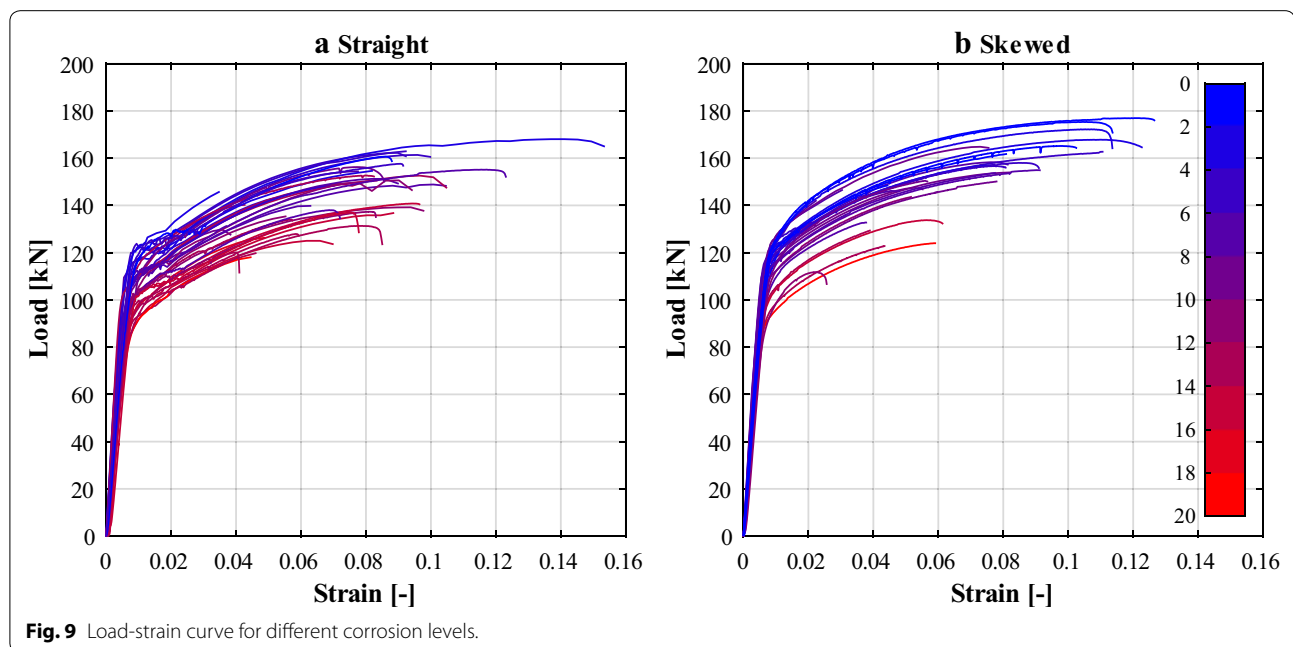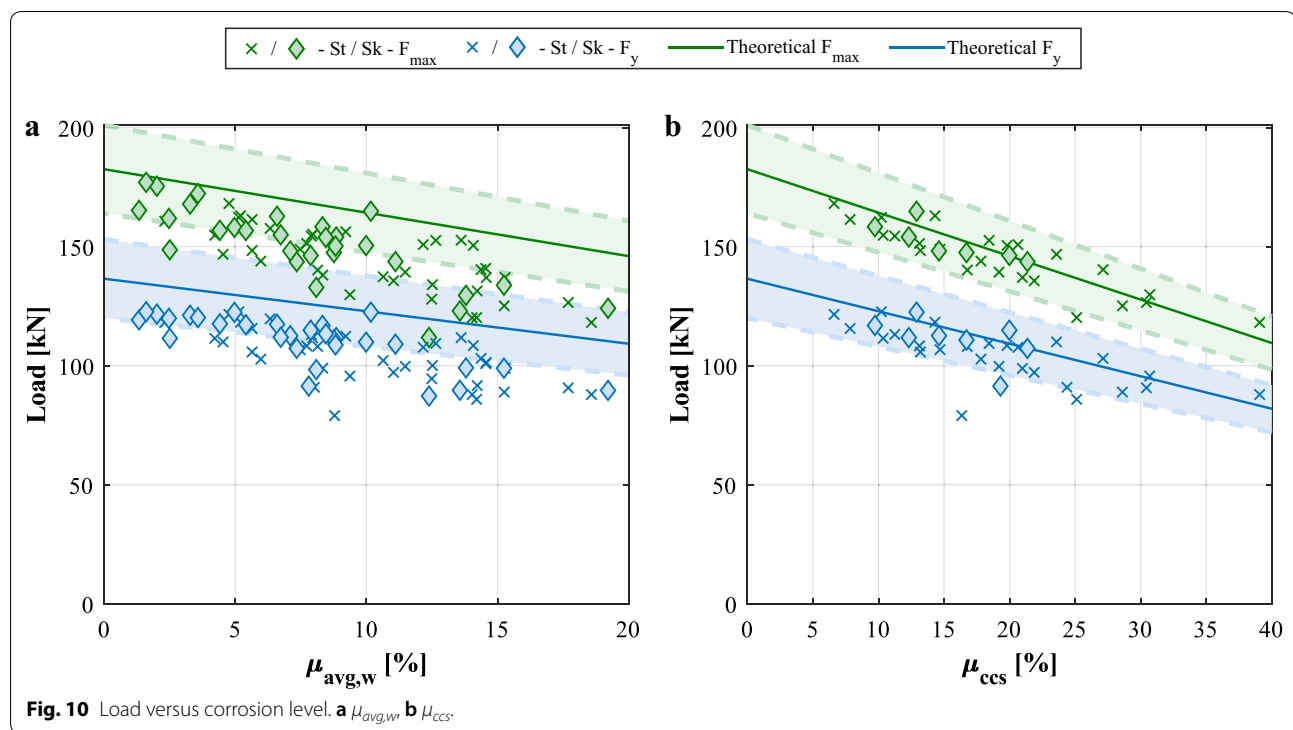
used, significantly higher values of α of up to 3.2, cf. (Santos and Henriques 2015; Bazán et al. 2016; Cobo et al. 2011), were found. The most likely reason for such discrepancy is that, in this work, the bars presented a homogeneous cross-sectional microstructure with uniform performance whereas the TEMPCORE® bars present a heterogenous microstructure formed by a ferrite core and an outer martensitic layer. Since the outer martensitic layer is the part of the cross-section providing a higher resistance, the fact that corrosion affects primarily the most external regions of the bar explains the greater degradation rate in TEMPCORE® bars.

Another important difference observed in this study with respect to the available research lies in the fact that the trend described by the results presented in Fig. 10a does not converge to the reference (uncorroded) load value as the corrosion level approaches zero. The explanation for this phenomenon can be found in the corrosion mechanisms: in most experimental studies, corrosion is promoted by impressing an electric current to the reinforcement bars whereby the entire exposed surface starts to corrode simultaneously. Conversely, in naturally corroded bars coming from real concrete structures, corrosion is more likely to start by very localized pitting at specific regions. Consequently, at early corrosion stages the average corrosion could be very limited yet the local loss of cross-sectional area at the critical pit could be significantly higher. This is supported by the relationship

between average corrosion and critical corrosion levels depicted in Fig. 8b. In addition, the experimental results of the ultimate and yielding load are plotted in Fig. 10b as a function of the critical corrosion level. As observed, in this case a good agreement is found between the experimental values and the theoretical load loss attributable to the reduction of cross-sectional area. Moreover, Fig. 10b also shows that almost all the experimental data points fall within the confidence bounds obtained for the computed theoretical load, which as previously mentioned assumes a normal distribution of the mechanical properties for the uncorroded bars as detailed in Table 3.

Based on the good agreement between the loss of load and the critical corrosion level, it can be inferred that the load capacity of a corroded bar with homogeneous material properties across its section can be described, to a large extent, in terms of the remaining cross-sectional area. In order words, α becomes 1 when μ in Eq. (2) represents the critical corrosion level. Subsequently, if a link between the average and critical corrosion levels could be established, then it should be possible to estimate the load at failure and the load at yielding of a corroded bar based solely on the $\mu_{avg,w}$ and the corresponding capacity of the uncorroded bar. Therefore, it can be hypothesised that by using Eq. (1), which relates such parameters, $\mu_{avg,w}$ to μ_{ccs}, an estimation of the load reduction due to corrosion for the different specimens should be possible.

Fig. 11 Comparison between Load measured at test and Load estimated through μ_{ccs} by Eq. 1.
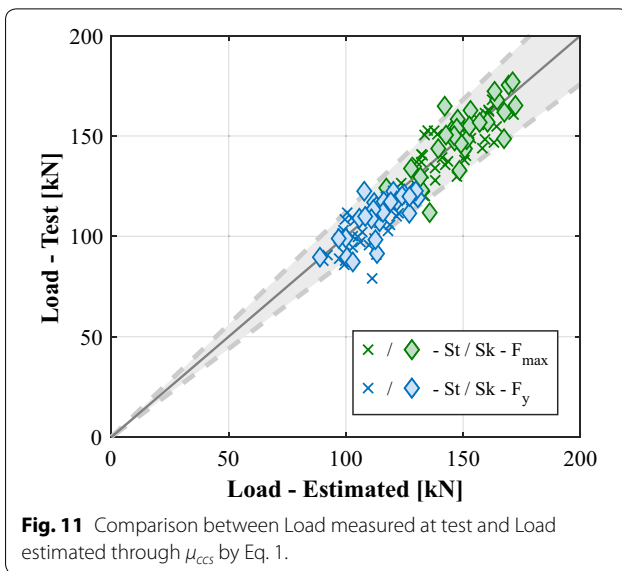
In order to validate that hypothesis, an evaluation of the load at failure and at yielding was carried out using the μ_{ccs} values predicted by Eq. (1). A comparison between the estimated and the experimental values from the tensile tests, for both Set-2 and Set 3, is presented in Fig. 11. As observed, most the points are distributed along the equality line and close to it, indicating a very good agreement. This becomes even more apparent when the natural scatter of the parameter, indicated in Fig. 11 as a grey stripe, is accounted for. Consequently, it

can be stated that the relation presented in Sect. 3, yields valid results for the estimation of the μ_{ccs} from weight loss measurements.

4.3 Ultimate and Yielding Strength

The calculation of the ultimate and yielding strength was performed as the ratio between the actual load measured from the tensile test and the cross-sectional area of the bar. Thus, depending on the considered cross-sectional area used in the calculations of the stresses, namely the mean uncorroded bar area ($A_{avg,unc}$), the average corroded area ($A_{avg,w}$) or the critical cross-section area (A_{ccs}), three different values are obtained. Accordingly, Fig. 12 presents the resulting calculated strength values as a function of the corresponding corrosion level: Fig. 12a, shows the stresses using the mean uncorroded area, Fig. 12b shows the stresses using the corresponding average corroded area of the each bar, while Fig. 12c displays the stresses calculated based on the critical cross-sectional area of each bar.

A clear trend can be seen in Fig. 12a where the apparent strength of the bar, calculated based on the mean uncorroded areas, shows a rapid degradation with increasing corrosion levels. The degradation of the bar strength is somewhat milder when the average corroded area is used. However, when the strength of the bar is computed based on the critical cross-sectional areas, the results not only remain within the confidence bounds associated to the natural scatter of the material, but they even exhibit

Fig. 12 Stress-corrosion level. **a** $A_{avg,unc}$, **b** $A_{avg,w}$ **c** A_{ccs}.
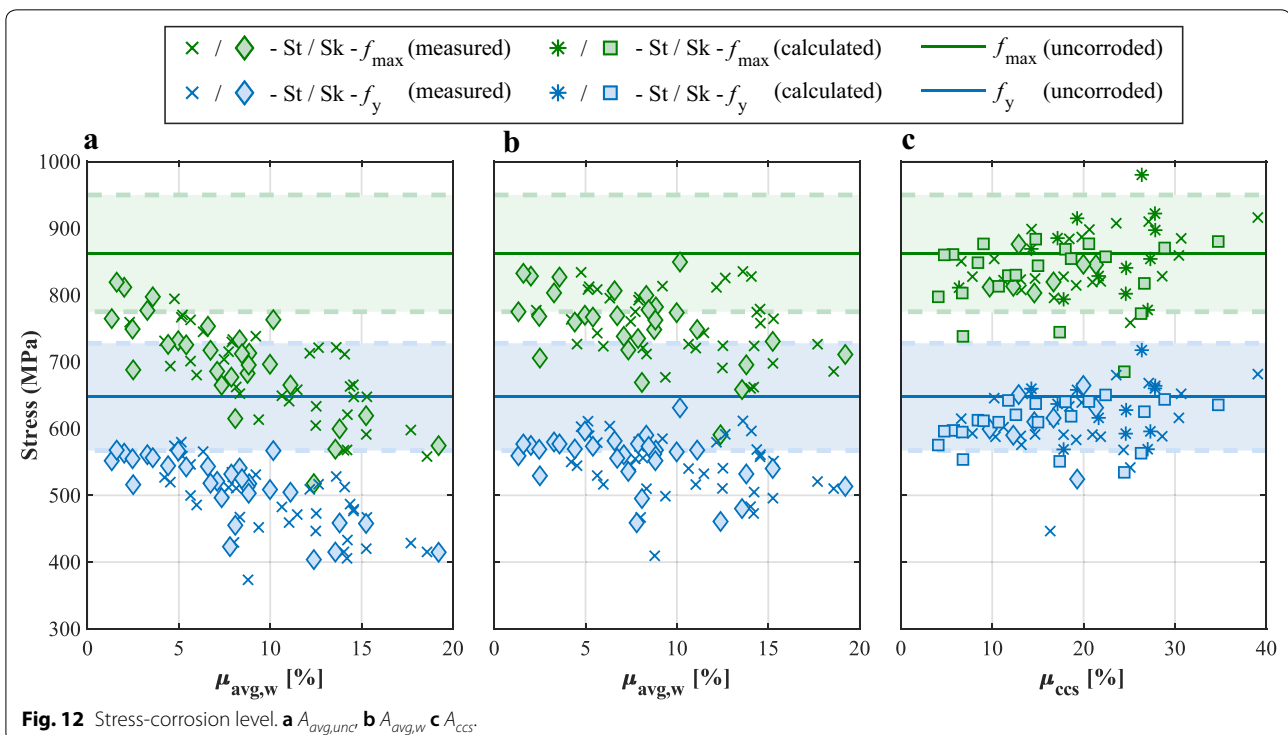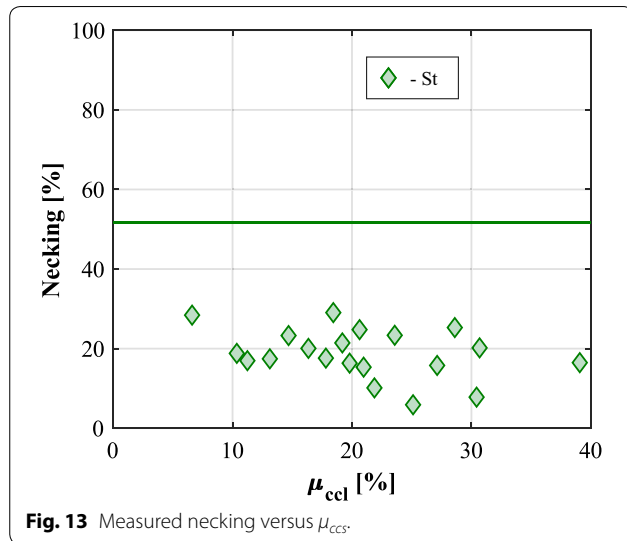
Fig. 13 Measured necking versus μ_{ccs}.

an inverted trend where the strength slightly increases with increasing corrosion levels. This observation indicates that the bar strength is independent of the corrosion level, as long as the internal microstructure of the bar is constant throughout the bar section, i.e. the bars a not TEMPCORE®. These findings are in line with the results by (Tang et al. 2014; Lu et al. 2016; Palsson and Mirza 2002) who also used the measured critical cross-sectional area to calculate the stress and found no loss in the bar strength associated to corrosion. Nevertheless, it should be noted that studies where the actual cross-sectional area is accurately measured and used to compute the stresses are very scarce and in the existing papers an explanation for this phenomenon is not provided.

A plausible explanation for the observed behaviour can be attributed to the local effects introduced by the geometrical differences in the pits. First of all, the existence of a pit in the bar suppresses, to a large extent, the necking effect commonly observed in uncorroded bars, i.e. the local reduction of cross-section after reaching the maximum load capacity. Figure 13 illustrates a clear non-linear relationship between necking and the critical corrosion level, where the necking has been determined as:

$$Necking = 1 - A_{ccs,f}/A_{ccs} \qquad (3)$$

where A_{ccs} and $A_{ccs,f}$ represent the critical cross-sectional area before and after testing, respectively. This behaviour is in contradiction with the linear trend reported by Lu et al. (2016). In this work, similar to the behaviour observed for the load, the reduction of necking exhibited a significant initial drop for low corrosion levels. A reduction of necking of at least 50% was observed for all the corroded bars with respect to the necking of uncorroded bars, regardless of the corrosion level.

As a result, corroded bars do not exhibit a descending branch after the peak load, see Fig. 9. Furthermore, due to the absence of necking, the apparent stresses measured when using the critical cross-sectional area are closer to the true stresses than when the nominal or uncorroded areas are used. Since the suppression of necking is accentuated for increasing corrosion levels, the measured trend displays an increasing bar strength for higher sectional losses. However, it should be noted that unlike for the uncorroded case where a nearly uniform stress distribution can be assumed in the bar's cross-section, the existence of the pit leads to two different second order effects that originate a non-uniform stress distribution around the pit section. As a result, the stress in a small region of the critical cross-section near the pit can reach very high values while the average is kept relatively low. Moreover, these second order effects, namely the local bending due to a shift in the centre of gravity and the stress concentration due to a sudden change in geometry, progress differently with increasing corrosion levels. As illustrated in Fig. 14, the pit depth increases for increasing corrosion levels, hence local bending effects become more relevant, whereas the pit depth to pit length ratio tends to decrease as the corrosion level rises, which makes the notch effect less pronounced.

4.4 Strain at Failure, Strain at Maximum Load and Strain at Yielding

The deformation capacity of the bars was negatively affected by corrosion even at moderate corrosion levels. However, contrary to what was shown in previous sections for loads and stresses, the measured strains did not exhibit a clear trend in relation to the corrosion level. Figure 15 presents the strain at failure, ε_u, the strain at maximum load, ε_{max}, and the strain at yielding, ε_y, as a function of the critical corrosion level, μ_{ccs}.

Even though a clear trend is not apparent, various noteworthy aspects were identified: (i) the ε_u decreased dramatically, more than 50% reduction, even for relatively low corrosion levels. This fact implies that the total deformation capacity of the bars, hence their ductility, is drastically affected even for critical corrosion levels lower than 10%. Conversely, the ε_{max} did not show such noticeable reduction for low corrosion levels; (ii) the difference between ε_u and ε_{max} became significantly less apparent in corroded bars. (iii) although most of the loss of ε_u occurs at very low corrosion levels (lower than 10% μ_{ccs}), a trend can be observed where strains continue decreasing for increasing corrosion levels, which can be also observed for ε_{max}. However, as already mentioned, such trend is considerably weaker than for other parameters; (iv) a non-negligible increase of ε_y was observed with

Fig. 14 Pit depth ratios as a function of the critical corrosion level: **a** to nominal diameter and **b** to pit length.
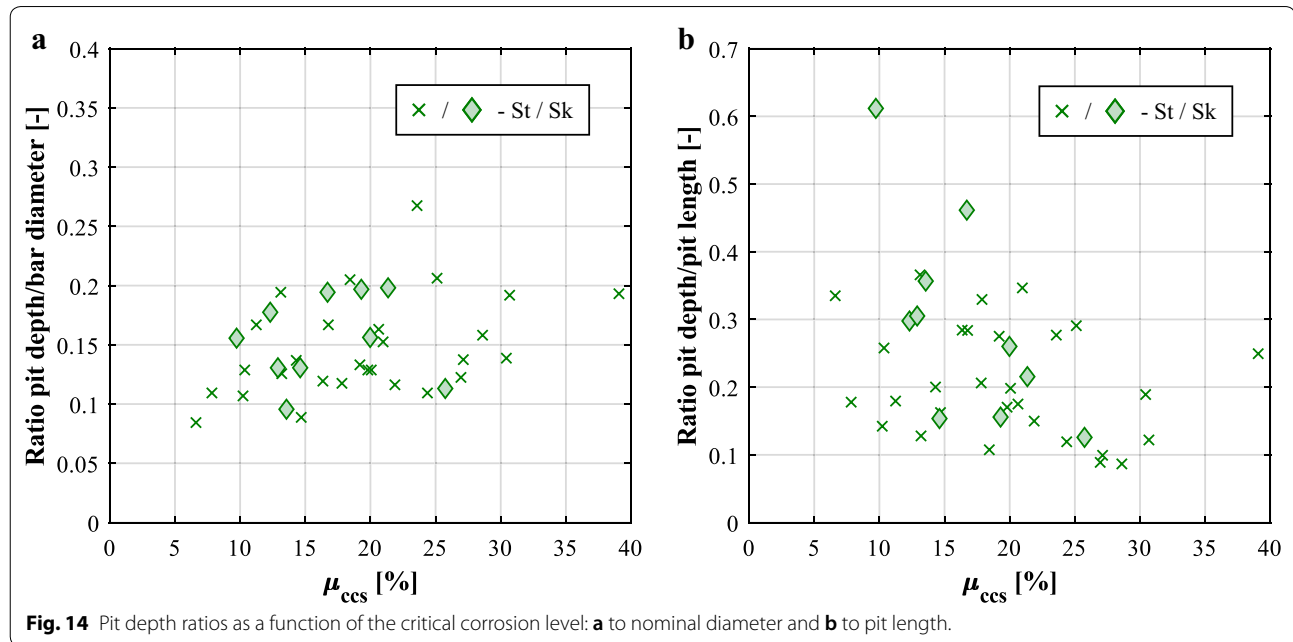
increasing corrosion, which can be explained by a reduction of the bar stiffness caused by the reduced cross-sectional area along the bar length. This is as well in line with previous studies (Fernandez et al. 2015; Almusallam 2001; Du et al. 2005).

Again, as it should be noted from Fig. 16, some of the aforementioned observations can be attributed to the loss of necking. Figure 16a clearly shows that the loss of ε_u follows a linear trend with respect to the loss of necking, while in Fig. 16b an evident parabolic trend between

the ε_u to ε_{max} ratio and the loss of necking is described, which also indicates that the convergence of the ε_{max} and ε_u, values in corroded bars is closely connected to the loss of necking. This finding, together with the results presented in Fig. 13, evidences the existence of a connection between three different phenomena: the critical corrosion level, the percentage of necking at failure and the reduction and confluence of ε_u and ε_{max}.

Even though a relationship between those phenomena is evident, an additional conclusion that can be inferred

Fig. 15 Strain-corrosion level (μ_{ccs}). **a** ε_{max} and ε_u, **b** ε_y.
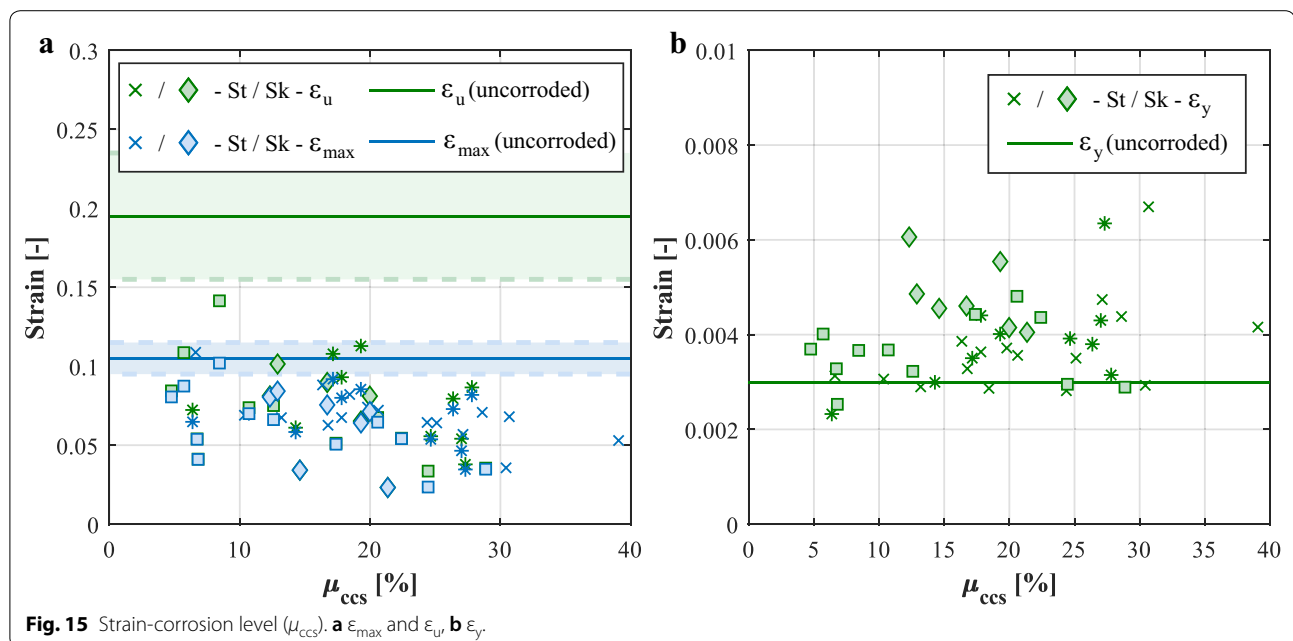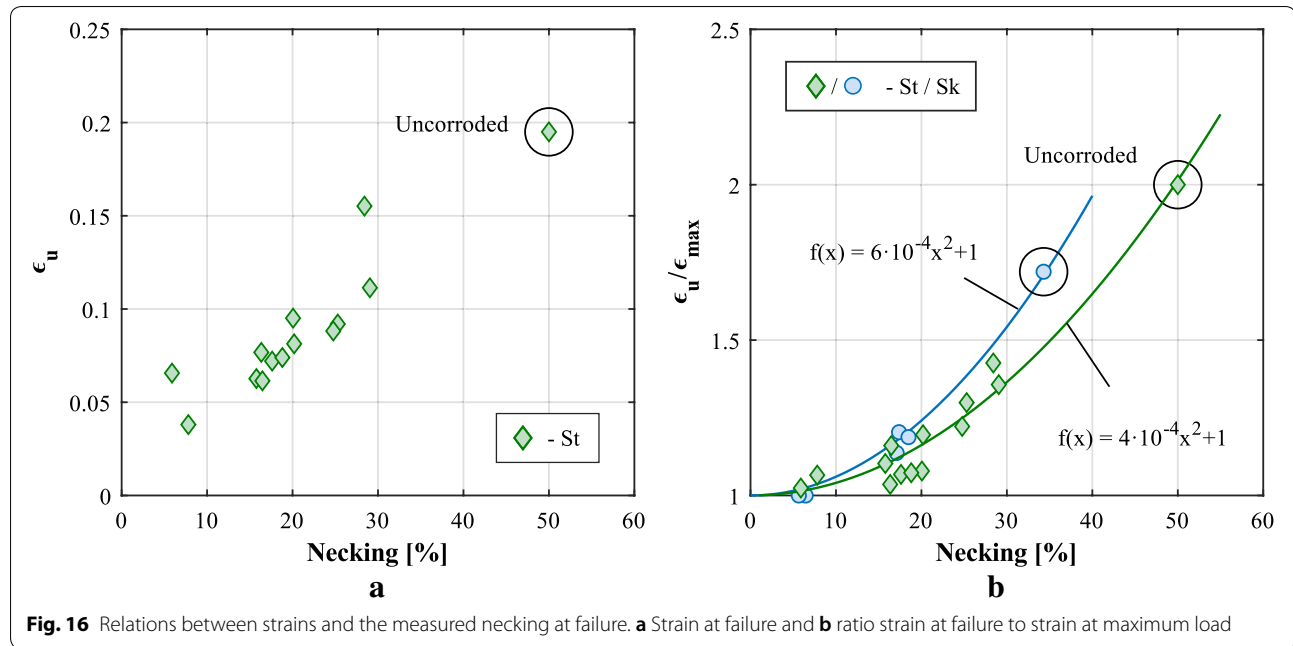
Fig. 16 Relations between strains and the measured necking at failure. **a** Strain at failure and **b** ratio strain at failure to strain at maximum load

from the weak trend found in Fig. 14a is that the remaining cross-sectional area in the bar is not the only factor governing the reduction in strain capacity ε_u or ε_{max} and the loss of necking. In order to investigate whether the shape of the pit could play an important role in the behaviour of the ε_u or ε_{max} and the necking of the bar at failure, the following pit shape factor, ψ, was defined:

$$\psi = u_{eq}/u_c = 2\sqrt{\pi A_{ccs}}/u_c \qquad (4)$$

where u_{eq} is the equivalent perimeter of the circle with area equal to the critical cross-sectional area, A_{ccs}, and

u_c represents the perimeter at the critical cross-section. This factor compares how the measured perimeter deviates from the theoretical perimeter of a circumference with the same cross-sectional area to provide a measure of how irregular the pit shape factor is. Therefore, a low pit shape factor indicates that corrosion at the critical cross-section tends to be governed by many large and deep pits, whereas a factor close to unity describes a more uniform corrosion. The factor ψ can theoretically adopt any value between 0 and 1 but in practice a lower bound larger than zero exist.
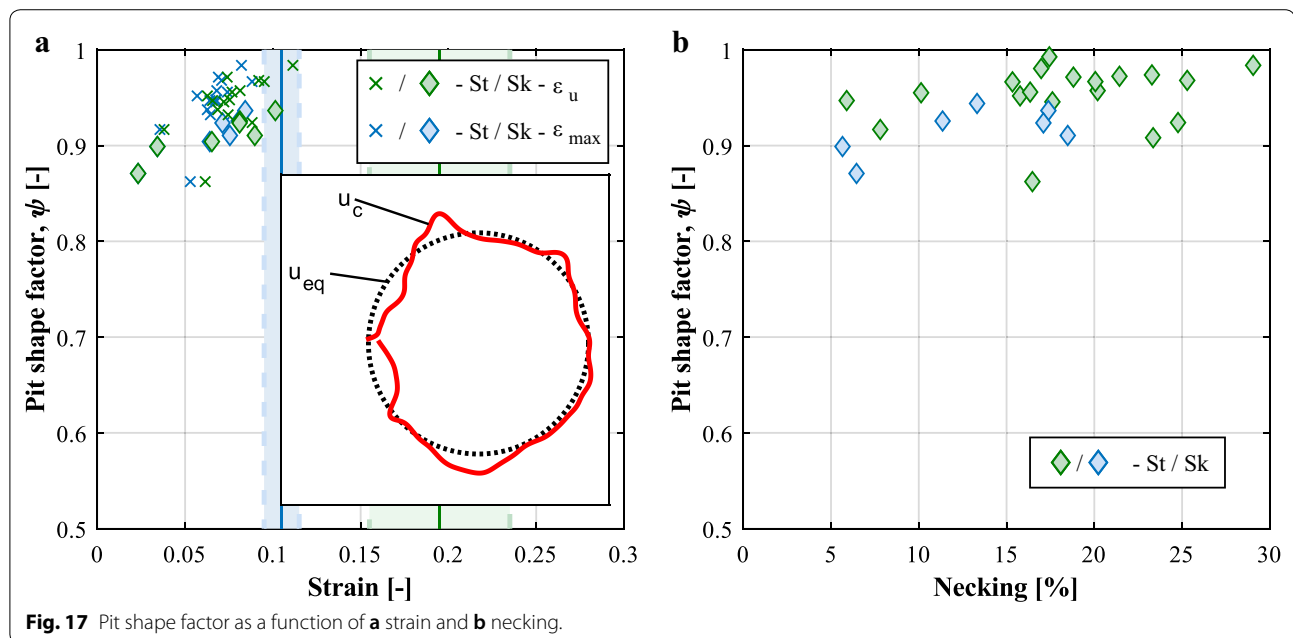
Fig. 17 Pit shape factor as a function of **a** strain and **b** necking.

Fig. 18 Normalised pit characteristics as function of normalised strains.
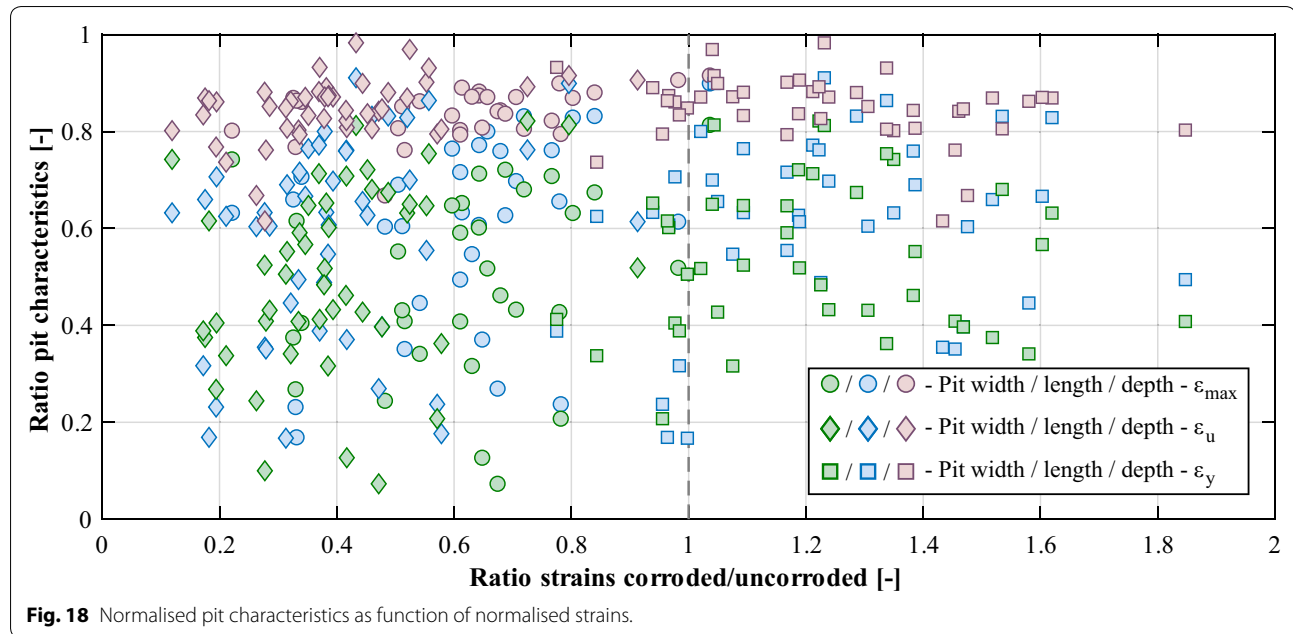
In Fig. 17a, the pit shape factor is plotted as a function of the measured strain together with a graphical representation of the actual and equivalent critical cross-sections. As observed, the trend between the presented shape factor and the loss of strain is more apparent than for the cross-sectional loss. A similar trend is observed in Fig. 17b, where the pit shape is plotted versus the measured necking. This seems to indicate that, indeed, the presence of deep pits and non-uniform corrosion, which increases the impact of the second order effects happening at the critical cross-section, might be the reason for a prematurely induced failure of the bar in terms of strain and necking capacity. Furthermore, the most noticeable effect is still the initial drop of strain for high shape factors, indicating that even very small pits are sufficient to produce a remarkable reduction of the strain capacity. Nevertheless, after such initial loss, the subsequent loss of strain progressed almost linearly with decreasing pit shape factors.

4.5 Effect of the pit characteristics on the deformation capacity of the bars

As mentioned in Section 4.4, the strain reduction was found to have a stronger link to the pit shape than to the actual critical corrosion level and the necking at failure. However, the pit at the critical cross-section can be also characterised by other parameters than the pit shape factor introduced, e.g. pit length, pit depth and pit width. Consequently, this section aims to describe the impact of the three main characterising parameters of a pit in the loss of strain capacity. Figure 17 illustrates the

influence of the individual pit features on the different strain measurements, where each pit characteristic has been normalized to a theoretical limit value according to Eq. (5) while the strains have been normalized to the corresponding uncorroded mean values, presented in Table 3. The theoretical limit for the pit depth and pit width were assumed as the nominal bar diameter, i.e. 16 mm. Although the length of a pit is only strictly limited by the bar length, in practice an upper threshold of about 2.5 times the nominal bar diameter, i.e. 40 mm, was observed in this work, which was also noticed by Fernandez et al. (2015).

$$L_{pit,n} = 1 - L_{pit}/2.5\emptyset_{nom} \quad (5.1)$$
$$D_{pit,n} = 1 - D_{pit}/\emptyset_{nom} \quad (5.2) \quad\quad (5)$$
$$W_{pit,n} = 1 - W_{pit}/\emptyset_{nom} \quad (5.3)$$

In line with what was indirectly noticed in the previous section, it is clearly concluded from the results expressed in Fig. 18 that the pit depth is the parameter which has the largest impact in the measured strain. A small increase in such magnitude implied a big reduction in the measured strain both at failure and maximum. Conversely, the opposite behaviour is observed for the yielding strain, where a small variation in the pit depth indicates an important increasing of the strain. This is well in line with the results presented in Section 4.4, and it is justified by the presence of second order effects that induce local yielding at the pit cross-section in earlier stages, while the remaining sections in the bar are still in the elastic range.

The other two parameters, the pit length and pit width, describe similar trends for the strain at failure and the

strain at maximum load. However, it is clearly seen that such trends are much weaker than for the pit depth, or in other words, the strain reduction is not so sensitive to the variation in length or width of the pit. Similarly, the strain at yielding did not seem to be so sensitive to the pit length and width either, where a large scatter is observed.

5 Conclusions

This paper reports experimental results of tensile tests carried out on naturally corroded reinforcing steel bars. Relations between the main mechanical parameters and both average and critical corrosion levels have been investigated. In addition, relations between physically measured parameters such as the pit shape or the loss of necking at failure and the loss of bar's ductility have been presented. Based on the results of the present study the following conclusions can be drawn:

(1) The loss of load, both ultimate and at yielding, was observed to follow a linear relationship with the corrosion level, where the scatter in the results fell within the natural variation of the uncorroded samples.

(2) When describing the load loss as a function of the average corrosion level, a greater loss than the attributable to the bar cross-sectional area reduction was obtained. Moreover, a sudden load drop at very small corrosion levels was observed in contrast to reported results by other researchers. This was attributed to a fundamental difference in the development of corrosion at early stages, where the application of an impressed current to accelerate corrosion leads to uniformly distributed pitting, whereas in naturally corroded bars, corrosion initiates by very localised pitting.

(3) The load loss described as a function of the critical corrosion level was in a very good agreement with the theoretical loss attributable to the reduction of cross-sectional area. Consequently, the residual load capacity of corroded bars may be solely ascribed to the remaining cross-sectional area at the critical pit.

(4) An expression was derived to predict the critical corrosion level in a bar from average corrosion measurements, based on the empirical relation observed between the average corrosion level and the corrosion level at the critical pit. The expression was used to successfully estimate the yield and ultimate load of a validation set of 51 bars.

(5) The evaluation of the yield and ultimate strength greatly depends on the cross-sectional area considered. Whereas a clear degradation of the strength was apparent when using the nominal and average corroded cross-sectional areas, using the actual cross-section at the critical pit resulted in a slightly increasing trend of the strength for higher corrosion levels due to the reduction of necking. Consequently, in the assessment of corroded structures, the characteristic strength may be used provided the critical cross-sectional area is considered.

(6) The deformation capacity of the bars was drastically affected by the existence of pits. In most cases, the ultimate strain, ε_u, suffered a severe reduction of more than 50% due to strain localisation in the pit, while the difference between ε_u and ε_{max} became almost negligible due to the loss of necking. Conversely, the strain at yielding, ε_y, displayed an increasing trend.

(7) Unlike for the load capacity, the loss of ultimate strain did not seem to be governed by the critical corrosion level alone. Through the definition of a pit shape factor, the shape of the cross-section at the critical pit and the loss of necking at failure were found to be better parameters to describe the loss of strain. Among the different pit features, the loss of strain was more sensitive to the pit depth whereas the length and depth of the pit exhibited a large scatter and therefore no clear influence.

Author details
[1] Division of Structural Engineering, Chalmers University of Technology, Göteborg 412 96, Sweden. [2] Thomas Concrete Group AB, Södra Vägen 28, Göteborg 412 54, Sweden.

Appendix A
See Tables 4, 5 and 6.

Table 4 Set number 1.

Bar #	Bar type	F_{max} (kN)	F_y (kN)	ε_{max} (–)	ε_u (–)	ε_y (–)
ST1-1	Sk	172.3	129.5	0.116	0.152	0.010
ST1-2	Sk	172.8	130.2	0.115	0.149	0.010
ST1-3	Sk	181.7	142.7	0.124	0.159	0.014
ST1-4	Sk	184.4	144.7	0.115	0.139	0.014
ST1-5	St	171.9	125.6	0.138	0.179	0.010
ST1-6	St	170.5	124.3	0.130	0.158	0.016
ST1-7	St	168.0	122.3	0.143	0.190	0.016
ST1-8	St	171.7	125.2	0.133	0.177	0.009
ST1-9	Sk	179.2	141.4	0.000	0.000	0.000
ST1-10	Sk	178.6	141.2	0.114	0.139	0.014
ST1-11	St	189.9	147.1	0.066	0.089	0.009
ST1-12	St	185.3	141.2	0.102	0.102	0.020
ST1-13	St	179.3	132.4	0.069	0.069	0.008
ST1-14	St	191.2	142.4	0.114	0.114	0.015
ST1-15	Sk	171.1	132.9	0.095	0.095	0.014
ST1-16	Sk	176.3	138.9	0.105	0.105	0.015
ST1-17	Sk	178.1	142.1	0.090	0.090	0.015
ST1-18	Sk	175.6	139.1	0.088	0.088	0.014
ST1-19	Sk	177.3	139.5	0.111	0.111	0.015
ST1-20	Sk	179.1	142.3	0.087	0.087	0.015
ST1-21	St	195.0	145.3	0.103	0.103	0.015
ST1-22	St	195.0	145.3	0.103	0.103	0.015
ST1-23	St	182.6	136.8	0.116	0.116	0.017
ST1-24	Sk	186.8	130.4	0.106	0.106	0.006
ST1-25	St	195.8	146.3	0.099	0.099	0.016
ST1-26	St	183.2	135.9	0.070	0.070	0.014
ST1-27	St	182.4	135.1	0.103	0.103	0.018
ST1-28	Sk	173.9	130.9	0.099	0.099	0.012
ST1-29	Sk	175.6	125.5	0.102	0.102	0.006
ST1-30	St	199.8	150.8	0.111	0.111	0.015
ST1-31	St	188.3	141.6	0.120	0.120	0.019
ST1-32	St	193.7	148.0	0.111	0.111	0.018
ST1-33	St	186.9	145.0	0.072	0.072	0.011
ST1-34	Sk	183.2	127.0	0.104	0.104	0.006
ST1-35	Sk	185.4	130.1	0.079	0.079	0.006
ST1-36	St	172.6	128.2	0.106	0.106	0.019
ST1-37	St	183.9	137.0	0.114	0.114	0.019
ST1-38	St	197.3	148.8	0.068	0.068	0.007
ST1-39	St	175.3	129.3	0.127	0.127	0.019
ST1-40	St	173.8	128.2	0.110	0.110	0.015
ST1-41	St	186.3	136.4	0.102	0.102	0.014
ST1-42	St	191.9	143.0	0.086	0.086	0.013
ST1-43	St	176.5	132.0	0.070	0.070	0.007

Table 5 Set number 2.

Bar #	Bar type	$\mu_{avg,w}$ (%)	A_{avg} (mm²)	Pit length (mm)	Pit width (mm)	Pit depth (mm)	F_{max} (kN)	F_y (kN)	ε_{max} (–)	ε_u (–)	ε_y (–)
ST2-1	St	13.61	182.79	–	–	–	152.7	115.6	0.080	0.087	0.010
ST2-2	St	14.03	181.91	25.8	14.4	6.15	120.1	94.2	0.039	0.041	0.010
ST2-3	St	9.21	192.11	32.94	10.2	3.12	156.2	113.6	0.077	0.086	0.012
ST2-4	Sk	1.33	213.17	5.5	4.3	1.94	165.2	122.3	0.098	0.103	0.010
ST2-5	Sk	6.59	201.80	12.55	5.61	2.77	162.7	120.7	0.111	0.113	0.011
ST2-6	Sk	6.73	201.49	12.4	6.88	1.53	154.9	116.1	0.091	0.095	0.011
ST2-7	Sk	2.50	210.64	15	10.6	4.21	148.6	122.3	0.045	0.048	0.012
ST2-8	Sk	–	216.04	–	–	–	185.7	141.9	0.101	0.115	0.011
ST2-9	Sk	–	216.04	–	–	–	178.0	141.7	0.137	0.164	0.021
ST2-10	Sk	–	216.04	–	–	–	174.9	137.6	0.136	0.159	0.017
ST2-11	Sk	4.97	205.31	13.85	7.33	1.52	158.0	126.3	0.086	0.091	0.011
ST2-12	Sk	0.89	214.11	6.18	6.72	1.31	177.3	139.3	0.140	0.164	0.017
ST2-13	Sk	–	216.04	–	–	–	180.6	143.6	0.147	0.182	0.020
ST2-14	Sk	4.41	206.51	20.46	8.26	2.77	156.9	120.4	0.075	0.079	0.011
ST2-15	Sk	8.09	198.57	15.85	12.09	5.31	132.9	110.4	0.038	0.038	0.010
ST2-16	Sk	13.56	186.73	12	6.01	3.36	123.0	98.4	0.044	0.044	0.010
ST2-17	Sk	3.28	208.96	9.51	2.85	1.72	167.8	123.8	0.110	0.126	0.011
ST2-18	Sk	19.21	174.53	36.16	8.55	4.11	124.1	95.2	0.059	0.062	0.010
ST2-19	Sk	13.80	186.23	30	9.07	3.2	129.5	105.6	0.039	0.039	0.011
ST2-20	Sk	15.25	183.10	33.24	6.15	2.18	133.8	104.5	0.057	0.064	0.010
ST2-21	Sk	11.11	192.04	25.95	9.46	3.81	143.7	115.2	0.052	0.052	0.012
ST2-22	Sk	8.45	197.78	64.83	8.84	1.69	153.9	116.4	0.078	0.081	0.010
ST2-23	Sk	8.82	196.98	16.51	6.36	3.01	150.2	112.5	0.078	0.078	0.010
ST2-24	Sk	5.40	204.37	18.12	10.94	2.05	156.7	120.3	0.078	0.084	0.010
ST2-25	Sk	1.39	213.04	9.43	3.1	0.84	188.4	134.6	0.145	0.164	0.012
ST2-26	Sk	9.99	194.46	13.34	6.93	2.07	150.4	117.1	0.056	0.061	0.011
ST2-27	Sk	–	216.04	–	–	–	187.9	133.8	0.154	0.204	0.011
ST2-28	Sk	–	216.04	–	–	–	190.6	135.1	0.157	0.191	0.012
ST2-29	Sk	–	216.04	–	–	–	188.6	134.5	0.156	0.205	0.011
ST2-30	St	12.52	185.11	15.81	9.1	2.37	134.0	104.5	0.057	0.060	0.011
ST2-31	St	14.55	180.81	13.77	9.16	1.61	140.8	103.0	0.095	0.097	0.011
ST2-32	St	7.95	194.77	17.81	5.65	1.57	155.2	111.9	0.117	0.126	0.011
ST2-33	St	14.22	181.50	30.74	11.71	3.71	131.4	98.6	0.078	0.085	0.012
ST2-34	St	6.11	198.67	22.46		7.41	81.8	75.0	0.014	0.016	0.009
ST2-35	St	8.34	193.96	24.11	9.65	2.45	138.0	104.5	0.069	0.072	0.011
ST2-36	St	10.64	189.09	20.5	6.13	3.01	137.4	104.5	0.082	0.085	0.011
ST2-37	St	12.49	185.17	37.81	9.11	3.3	127.9	99.5	0.059	0.062	0.012
ST2-38	St	14.57	180.77	26.78	10.23	2.32	137.0	104.8	0.076	0.080	0.016
ST2-39	St	2.31	206.72	24.47	9.4	1.08	160.7	120.2	0.085	0.091	0.012
ST2-40	St	6.33	198.21	33.31	7.91	2.42	157.6	121.6	0.091	0.094	0.011
ST2-41	St	–	211.60	–	–	–	173.5	127.2	0.163	0.202	0.020
ST2-42	St	–	211.60	–	–	–	166.4	120.4	0.154	0.203	0.020
ST2-43	St	–	211.60	–	–	–	173.1	127.4	0.168	0.218	0.021
ST2-44	St	–	211.60	–	–	–	172.2	126.8	0.177	0.237	0.021
ST2-45	St	–	211.60	–	–	–	173.7	128.0	0.169	0.206	0.021
ST2-46	Sk	12.39	189.28	27.33	9.78	2.65	111.8	99.4	0.022	0.026	0.010
ST2-47	Sk	3.57	208.32	5.14	5.5	0.98	172.3	126.3	0.106	0.114	0.011
ST2-48	Sk	2.01	211.70	5.44	3.93	1.1	175.4	127.8	0.106	0.117	0.011
ST2-49	Sk	1.60	212.59	3.56	3	0.27	177.0	126.3	0.120	0.127	0.011
ST2-50	Sk	2.47	210.71	14.69	7.61	1.9	161.8	123.7	0.081	0.081	0.011
ST2-51	Sk	0.71	214.50	12	5.6	0.49	173.6	127.0	0.128	0.134	0.011

Table 6 Set number 3.

Bar #	Bar type	$\mu_{avg,w}$ (%)	A_{avg} (mm²)	A_{ccs} (mm²)	$\mu_{avg,3D}$ (%)	μ_{ccs} (%)	Pit length (mm)	Pit width (mm)	Pit depth (mm)	F_{max} (kN)	F_y (kN)	ε_{max} (−)	ε_u (−)	ε_y (−)
ST3-1	St	7.90	194.88	187.81	5.94	11.24	14.88	8.11	2.67	154.4	115.9	0.077	0.081	0.009
ST3-2	St	9.37	191.77	146.67	13.56	30.68	25.17	13.97	3.07	129.8	105.3	0.036	0.039	0.008
ST3-3	Sk	8.85	196.92	189.45	7.44	12.31	9.54	4.67	2.84	154.0	115.6	0.084	0.084	0.009
ST3-4	Sk	7.34	200.18	169.90	7.83	21.36	14.71	4.12	3.17	143.7	121.5	0.024	0.024	0.009
ST3-5	St	13.84	182.31	173.77	10.68	17.88	7.83	5.22	2.58	153.6	123.6	0.030	0.031	0.010
ST3-6	Sk	7.10	200.71	184.47	4.04	14.61	13.61	10	2.09	148.2	124.8	0.033	0.033	0.009
ST3-7	Sk	10.17	194.07	188.17	8.51	12.90	6.85	5.89	2.09	164.9	122.1	0.074	0.079	0.009
ST3-8	Sk	8.32	198.05	195.02	5.87	9.73	4.07	3.38	2.49	158.3	119.9	0.078	0.082	0.009
ST3-9	St	5.13	200.74	189.97	4.43	10.2	12.02	7.32	1.71	162.3	123.5	0.089	0.095	0.014
ST3-10	Sk	8.76	197.12	179.94	7.67	16.71	6.74	5.11	3.11	147.5	116.4	0.053	0.057	0.009
ST3-11	St	4.53	202.01	161.71	6.48	23.58	15.46	11.4	4.28	146.0	120.0	0.026	0.027	0.007
ST3-12	Sk	7.87	199.03	172.88	11.47	19.98	9.61	8.61	2.5	146.3	122.0	0.047	0.049	0.010
ST3-13	St	14.37	181.19	154.19	16.09	27.13	22.15	10.54	2.2	140.3	107.3	0.042	0.045	0.008
ST3-14	St	14.08	181.82	169.70	15.50	19.80	12.09	9.08	2.06	150.5	111.8	0.084	0.085	0.012
ST3-15	St	5.64	199.66	195.02	3.54	7.83	9.84	4.78	1.75	161.4	118.9	0.095	0.106	0.013
ST3-16	St	8.14	194.38	176.11	8.80	16.77	9.41	5.64	2.67	140.2	111.7	0.062	0.064	0.014
ST3-17	St	5.97	198.96	173.91	5.55	17.81	9.12	4.59	1.88	143.9	112.9	0.056	0.057	0.013
ST3-18	St	7.47	195.79	180.52	8.30	14.69	8.74	3.25	1.42	148.9	110.7	0.100	0.110	0.012
ST3-19	St	14.20	181.55	158.46	15.72	25.11	11.35	6.54	3.3	120.2	95.0	0.048	0.049	0.013
ST3-20	St	12.65	184.84	172.59	14.46	18.44	30.51	12.68	3.28	152.6	113.3	0.097	0.108	0.014
ST3-21	St	7.72	195.25	183.83	6.72	13.12	8.5	5.34	3.11	151.3	111.7	0.083	0.091	0.012
ST3-22	St	11.48	187.31	170.99	10.45	19.19	7.74	5.85	2.13	139.3	104.8	0.090	0.101	0.012
ST3-23	St	5.64	199.67	183.68	6.10	13.19	15.71	6.37	2.01	148.3	113.7	0.070	0.072	0.015
ST3-24	St	4.76	201.53	197.61	1.79	6.61	4.03	2.98	1.35	168.1	121.9	0.138	0.159	0.017
ST3-25	St	11.03	188.25	165.31	9.80	21.88	12.41	7.38	1.86	135.6	105.4	0.058	0.060	0.013
ST3-26	St	17.70	174.15	147.20	18.31	30.43	11.74	9.52	2.22	126.5	100.8	0.048	0.052	0.013
ST3-27	St	5.20	200.60	181.33	7.68	14.31	10.94	5.77	2.19	163.0	121.4	0.094	0.099	0.014
ST3-28	St	4.22	202.68	189.69	3.76	10.36	7.99	7.72	2.06	154.8	117.3	0.083	0.085	0.013
ST3-29	St	15.29	179.25	167.22	15.65	20.97	7.04	4.66	2.44	137.0	100.2	0.090	0.092	0.014
ST3-30	St	15.26	179.32	151.07	15.48	28.61	29.22	14.83	2.53	125.1	95.8	0.064	0.073	0.012
ST3-31	St	18.58	172.28	128.92	25.55	39.07	12.39	7.16	3.09	118.1	95.2	0.045	0.049	0.013
ST3-32	St	12.17	185.86	167.94	12.38	20.64	14.91	4.46	2.61	150.8	110.5	0.088	0.094	0.012

μ_{avg} average corrosion level, A_{avg} average corroded area, A_{ccs} critical cross-section, μ_{ccs} critical corrosion level.

References

Almusallam, A. A. (2001). Effect of degree of corrosion on the properties of reinforcing steel bars. *Construction and Building Materials, 15,* 361–368. https://doi.org/10.1016/s0950-0618(01)00009-5.

Apostolopoulos, C. A. (2007). Mechanical behavior of corroded reinforcing steel bars S500s tempcore under low cycle fatigue. *Construction and Building Materials, 21,* 1447–1456. https://doi.org/10.1016/j.conbuildmat.2006.07.008.

Apostolopoulos, C. A., Demis, S., & Papadakis, V. G. (2013). Chloride-induced corrosion of steel reinforcement—Mechanical performance and pit depth analysis. *Construction and Building Materials, 38,* 139–146. https://doi.org/10.1016/j.conbuildmat.2012.07.087.

Apostolopoulos, C. A., & Papadakis, V. G. G. (2008). Consequences of steel corrosion on the ductility properties of reinforcement bar. *Construction and Building Materials, 22,* 2316–2324. https://doi.org/10.1016/j.conbuildmat.2007.10.006.

Apostolopoulos, C. A., Papadopoulos, M. P., & Pantelakis, S. G. (2006). Tensile behavior of corroded reinforcing steel bars BSt 500s. *Construction and Building Materials, 20,* 782–789. https://doi.org/10.1016/j.conbuildmat.2005.01.065.

ASTM G1 (2011) Standard practice for preparing, cleaning, and evaluating corrosion test. https://doi.org/10.1520/g0001-03r11.2.

Bazán, A. M., Cobo, A., & Montero, J. (2016). Study of mechanical properties of corroded steels embedded concrete with the modified surface length. *Construction and Building Materials, 117,* 80–87. https://doi.org/10.1016/j.conbuildmat.2016.04.109.

Cairns, J., Plizzari, G. A., Du, Y., Law, D. W., & Franzoni, C. (2005). Mechanical properties of corrosion-damaged reinforcement simulated pitting damage, test. *ACI Materials Journal, 102-M29,* 256–264.

Caprili, S., Salvatore, W., Valentini, R., Ascanio, C., & Luvarà, G. (2018). A new generation of high-ductile dual-phase steel reinforcing bars. *Construction and Building Materials, 179,* 66–79. https://doi.org/10.1016/j.conbuildmat.2018.05.181.

Cobo, A., Moreno, E., & Cánovas, M. F. (2011). Variación de las características mecánicas de armaduras de alta ductilidad B500SD en función de su grado de corrosión. *Materiales de construcción, 61,* 517–532. https://doi.org/10.3989/mc.2011.61410.

Du, Y. G., Clark, L. A., & Chan, A. H. C. (2005). Effect of corrosion on ductility of reinforcing bars. *Magazine of Concrete Research, 57,* 407–419.

Fernandez, I., Bairán, J. M., & Marí, A. R. (2015). Corrosion effects on the mechanical properties of reinforcing steel bars. Fatigue and σ–ε behavior. *Construction and Building Materials, 101,* 772–783. https://doi.org/10.1016/j.conbuildmat.2015.10.139.

Fernandez, I., Bairán, J. M., & Marí, A. R. (2016a). 3D FEM model development from 3D optical measurement technique applied to corroded steel bars. *Construction and Building Materials, 124,* 519–532. https://doi.org/10.1016/j.conbuildmat.2016.07.133.

Fernandez, I., Bairán, J. M., & Marí, A. R. (2016b). Mechanical model to evaluate steel reinforcement corrosion effects on σ-ε and fatigue curves. Experimental calibration and validation. *Engineering Structures.* https://doi.org/10.1016/j.engstruct.2016.03.055.

Fernandez, I., Zandi Hanjari, K., & Lundgren, K. (2018). Evaluation of the corrosion level of naturally corroded bars using different cleaning methods, CT and 3D scanning. *Materials and Structures, 51,* 1–28. https://doi.org/10.1617/s11527-018-1206-z.

Imperatore, S., Rinaldi, Z., & Drago, C. (2017). Degradation relationships for the mechanical properties of corroded steel rebars. *Construction and Building Materials, 148,* 219–230. https://doi.org/10.1016/j.conbuildmat.2017.04.209.

S.S. Institudes, Armeringsstång (1971). Kamstång Ks 60 och Ks 60S (STD-1250), pp 1–4. http://www.sis.se/byggnadsmaterial-och-byggnader/byggnadsstommar/betongkonstruktioner/sis-212515.

Lu, C., Yuan, S., Cheng, P., & Liu, R. (2016). Mechanical properties of corroded steel bars in pre-cracked concrete suffering from chloride attack. *Construction and Building Materials, 123,* 649–660. https://doi.org/10.1016/j.conbuildmat.2016.07.032.

Lundgren, K., Tahershamsi, M., Zandi, K., & Plos, M. (2015). Tests on anchorage of naturally corroded reinforcement in concrete. *Materials and Structures, 48,* 2009–2022. https://doi.org/10.1617/s11527-014-0290-y.

Palsson, R., & Mirza, M. S. (2002). Mechanical response of corroded steel reinforcement of abandoned concrete bridge. *Structural Journal, 99,* 157–162. https://doi.org/10.14359/11538.

Santos, J., & Henriques, A. A. (2015). Strength and ductility of damaged tempcore rebars. *Procedia Engineering, 114,* 800–807. https://doi.org/10.1016/J.PROENG.2015.08.029.

Tahershamsi, M., Fernandez, I., Lundgren, K., & Zandi Hanjari, K. (2016). Investigating correlations between crack width, corrosion level and anchorage capacity. *Structure and Infrastructure Engineering, 2479,* 1–14. https://doi.org/10.1080/15732479.2016.1263673.

Tahershamsi, M., Fernandez, I., Zandi, K., & Lundgren, K. (2017). Four levels to assess anchorage capacity of corroded reinforcement in concrete. *Engineering Structures, 147,* 434–447. https://doi.org/10.1016/j.engstruct.2017.06.024.

Tahershamsi, M., Zandi, K., Lundgren, K., & Plos, M. (2014). Anchorage of naturally corroded bars in reinforced concrete structures. *Magazine of Concrete Research, 66,* 729–744. https://doi.org/10.1680/macr.13.00276.

Tang, F., Lin, Z., Chen, G., & Yi, W. (2014). Three-dimensional corrosion pit measurement and statistical mechanical degradation analysis of deformed steel bars subjected to accelerated corrosion. *Construction and Building Materials, 70,* 104–117. https://doi.org/10.1016/j.conbuildmat.2014.08.001.

UNE-EN-ISO-15630-01:2011 (2011). Steel for reinforced and prestresed concrete—testing methods. Part 1: Bars and wires for reinforced concrete

VXElements-Creaform, (n.d.). https://www.creaform3d.com/en/metrology-solutions/3d-applications-software-platforms. Accessed Sept 2018

Zhang, W., Song, X., Gu, X., & Li, S. (2012). Tensile and fatigue behavior of corroded rebars. *Construction and Building Materials, 34,* 409–417. https://doi.org/10.1016/j.conbuildmat.2012.02.071.

Zhu, W., & François, R. (2014). Experimental investigation of the relationships between residual cross-section shapes and the ductility of corroded bars. *Construction and Building Materials, 69,* 335–345. https://doi.org/10.1016/j.conbuildmat.2014.07.059.

Zhu, W., François, R., Coronelli, D., & Cleland, D. (2013). Effect of corrosion of reinforcement on the mechanical behaviour of highly corroded RC beams. *Engineering Structures, 56,* 544–554. https://doi.org/10.1016/j.engstruct.2013.04.017.

Zhu, W., François, R., Poon, C. S., & Dai, J.-G. (2017). Influences of corrosion degree and corrosion morphology on the ductility of steel reinforcement. *Construction and Building Materials, 148,* 297–306. https://doi.org/10.1016/J.CONBUILDMAT.2017.05.079.